# Revision 2:

# Multi-scale and multi-modal imaging study of mantle xenoliths and petrological implications

Venier M.[1*], Ziberna L.[1], Mancini L.[2], Kao A.P.[3], Bernardini F.[4,5], Roncoroni G.[1], Milani S.[6], Youbi N.[7,8,9], Majigsuren Y.[10], De Min A.[1], Lenaz D.[1]

[1] Department of Mathematics and Geosciences, University of Trieste, Trieste, Italy.
[2] Slovenian National Building and Civil Engineering Institute, Ljubljana, Slovenia.
[3] Elettra Sincrotrone Trieste S.C.p.A., S.S. 14 Area Science Park, 34149 Basovizza, Trieste, Italy.
[4] Centro Fermi, Museo Storico della Fisica e Centro di Studi e Ricerche Enrico Fermi, Rome, Italy.
[5] Multidisciplinary Laboratory, The "Abdus Salam" International Centre for Theoretical Physics, Strada Costiera 11, 34014 Trieste, Italy.
[6] Department of Earth Science 'Ardito Desio', University of Milan, Milan, Italy.
[7] Department of Geology, Faculty of Sciences-Semlalia, Cadi Ayyad University, Marrakesh, Morocco.
[8] Instituto Dom Luiz, University of Lisbon, Lisbon, Portugal.
[9] Faculty of Geology and Geography, Tomsk State University, Tomsk, Russia.
[10] Geoscience Center, School of Geology and Mining, Mongolian University of Science and Technology, Ulaanbaatar, Mongolia.
*Corresponding author

## Abstract

The accurate textural characterization of mantle xenoliths is one of the fundamental steps to understanding the main processes occurring in the upper mantle, such as sub-solidus recrystallization, magmatic crystallization and metasomatism. Texture, composition, and mineralogy reflect the temperature, pressure, stress conditions, melting and/or contamination events undergone before and during the entrapment in the host magma. For these reasons, characterizing the three-dimensional (3D) texture of silicate, oxide, sulfide and glass phases has great importance in the study of mantle xenoliths. We performed a multi-scale and multi-modal 3D textural analysis based on X-ray computed microtomography (μ-CT) data of three mantle xenoliths from different geodynamic settings (i.e. mobile belt zone, pericraton, oceanic hotspot). The samples were selected to represent different, variably complex, internal structures, composed of grains of different phases, fractures, voids and fluid inclusions of different sizes. We used an approach structured in increasing steps of spatial and contrast resolution, starting with in-house X-ray μ-CT imaging (working at spatial resolution from 30 μm down to 6.25 μm) and moving to high-resolution synchrotron X-ray μ-CT at the micron scale.

We performed a 3D characterization of mantle xenoliths comparing the results with the analysis of conventional 2D images (thin sections) obtained by optical microscopy and simulating the random sectioning of several thin sections to estimate the probability of correct modal classification. The 3D models allow to extract textural information that cannot be quantified solely from thin sections: spinel layering, distribution of silicic glass and related vesicles. Moreover, high-density volumes identified as sulfides were detected in two xenoliths, showing no relation with the spinel layering in one case and a preferential concentration along fractures in the other. Given the variety of textures and mineral assemblages of mantle xenoliths worldwide, the results are used to suggest experimental and analytical protocols for the characterization of these materials.

*Keywords: 3D microcomputed tomography; X-ray synchrotron-based μ-CT; mantle xenoliths; petrology.*

# 1 Introduction

Investigating mantle xenoliths allows to better constrain the nature of the lithosphere, the mechanisms that generate melts in the mantle, as well as the evolution of the lithosphere beneath regions where no samples have been exposed by tectonic activity (e.g., Ringwood 1991; Coltorti et al. 2000; Pearson et al. 2003; Kiseeva et al. 2017). The composition, mineral assemblage and textures of mantle xenoliths reflect the temperature, pressure, stress conditions and melting or contamination events experienced before or during the entrapment in the host magma (Pearson et al. 2003). Studying the distribution of small-volume melts like glassy patches and veins, as well as the texture of silicate, oxide and sulfide phases in samples from the upper mantle has great potential for the study of mantle metasomatism (Coltorti et al. 2000; Hughes et al. 2016; Blanks et al. 2020).

In a conventional thin section of an anisotropic and/or inhomogeneous rock, the resulting two-dimensional (2D) texture depends on the orientation of the random sectioning plane. In some cases, this might hamper the appropriate characterization of the rock leading to poorer characterization of internal structures (like quenched melt channels, stress-driven fractures or voids, preferential distribution of some minerals, etc.) that bear important information about the processes occurring at depths. Extending the textural analysis of mantle xenoliths to the three-dimensional (3D) is a potentially powerful tool in Earth science (Carlson 2006).

Among analytical methods for 3D imaging of geological samples, X-ray computed microtomography (μ-CT), being a non-destructive technique, has significant value (e.g., Baker et al. 2012a; Cnudde and Boone 2013; Kyle and Ketcham 2015). It allows to determine the volumetric ratios and 3D spatial distribution of different minerals, glasses and voids (Ketcham and Carlson 2001, Hidas et al. 2007; Baker et al. 2012b; Polacci et al. 2015; Arzilli et al. 2017; Yao et al. 2020).

In previous studies of mantle xenoliths, in-house and synchrotron-based μ-CT techniques have been used, for example, to map 3D networks of interconnected glass (Troll et al. 2012; Patkó et al. 2020), reveal the distribution of fluid inclusions (Créon et al. 2017), determine shape and dimensions of spinel-pyroxene clusters and the variability of spinel textures (Bhanot et al. 2017) and quantify the distribution of geologically and economically important minerals (e.g., diamonds and sulfides; Howarth et al. 2015; Logvinova et al. 2015).

Considering a xenolith suite from a given locality, μ-CT may provide even more insights if it was systematically applied before any destructive analytical technique, allowing for a primary characterization of possible textural and/or mineral assemblage heterogeneity. Despite its potential, the technique is rarely used by the petrological community studying mantle xenoliths, possibly due to the limited access to such facilities. However, given the variability of size and X-ray attenuation coefficients of the phases within mantle xenoliths, it may also reflect the lack of a protocol providing appropriate instrumental and processing workflow.

This work investigates some specific petrological features of mantle xenoliths through μ-CT using a multi-scale approach. We performed a 3D textural analysis of three mantle xenoliths from different geodynamic settings. Due to the high complexity of their internal structure, we used an experimental protocol structured to sequentially increase spatial and contrast resolution. We started with μ-CT imaging based on in-house sources and then we moved to a synchrotron facility to achieve a higher contrast between the different phases and a spatial resolution at the micron scale.

# 2 Materials and Methods

## 2.1 Sample selection and geological background

| Sample | Provenance | Dimensions (mm) | Description | Related magmatism |
|---|---|---|---|---|
| MG10x | Mandalgovi, Mongolia | 45 x 37 x 21 | Coarse grained peridotite | Alkali basalt |
| Bi4 | Bou-Ibalrhatene, Morocco | 50 x 40 x 20 | Coarse grained peridotite, crumbly | Alkali basalt |
| FN38 | Fernando de Noronha, Brazil | 48 x 19 x 13 | Coarse grained peridotite, glass-bearing | Basanite |

*Table 1: Sample description*

We selected three mantle xenoliths from alkali basalts and basanites (Table 1). Mantle xenolith MG10x comes from a volcanic edifice (45°38’55.56N; 106°22’19.38E) south of Mandalgovi, Sajncagaan District, Central Mongolian plateau. The edifice belongs to an Upper Cretaceous - Eocene volcanic district (Yarmolyuk et al. 2019) located along the Mongol-Okhotsk Suture, which is related to the closure of the Mongol-Okhotsk Ocean around middle Jurassic times (Sheldrick et al. 2020). Since the crustal thickness in this area is ca. 45 km (Guy et al.,2014), it is estimated that the depth of provenance of this xenolith is greater than 45 km. The original xenolith size was approximately 45x37x21 $mm^3$ and no deformation structures, mineral layering or other inhomogeneity were visible in hand samples.

Xenolith Bi4 comes from the Bou-Ibalrhatene maar (33°20’11.52N; 5°3’24.16W), middle Atlas basaltic province, Morocco. In this locality, mantle xenoliths are found in Plio-Quaternary alkaline maar deposits and are porphyroclastic to protogranular spinel-lherzolites, sampled at depths from 30 to 40 Km (Lenaz et al. 2014). They are characterized by a broad range of chemical heterogeneities testifying to the metasomatized nature of the upper mantle in the pericratonic area of Morocco (Lenaz et al. 2014, 2019; Chanouan 2017), where pericratonic refers to an area bordering the West African Craton. The sample size was approximately 40x10x9 $mm^3$ and was a piece cut from a larger xenolith embedded in the host basalt. A major fracture was visible, but no mineral layering or any other inhomogeneity were visible in hand sample.

The FN38 xenolith comes from a basanite flow of the Sao José formation (3°49’36.9S; 32°24’05.5W), Sao José island, NW of the Brazilian archipelago of Fernando de Noronha. These basanites include abundant peridotitic xenoliths and have $^{40}Ar/^{39}Ar$ ages in the range 9.0 ± 0.2 to 9.5 ± 0.4 Ma (Perlingeiro et al. 2013; Lopes et al. 2015). The archipelago has a NE-SW trending course and belongs to the vast volcanic edifice positioned along the Fernando de Noronha ridge, which is interpreted as an OIB from a plume (Fodor et al. 1998; Lopes et al. 2015). Previous studies on the Fernando de Noronha mantle xenoliths suggested that they have been sampled from the depth range of 30–75 Km (Princivalle et al. 1994; Rivalenti et al. 2000). The original sample size was approximately 48x19x13 $mm^3$. No deformation structures, mineral layering or other inhomogeneity were visible in hand sample.

## 2.2 Experimental steps

Xenolith petrography was characterized through polarized light microscopy of thin sections and by X-ray computed microtomography (μ-CT). For each sample, the characterization by μ-CT included three or four steps with increasing spatial and contrast resolution.

Step A used cone-beam polychromatic μ-CT imaging at the Multidisciplinary Laboratory (MLab) of the Abdus Salam International Centre for Theoretical Physics (ICTP, Trieste, Italy) (Tuniz et al. 2013). In this step, the full volume for each sample was analyzed, to obtain a 3D reconstruction of the full xenolith microstructure. The tomographic scanning of all specimens was carried out using a sealed microfocus X-ray source (Hamamatsu L8121-03) at a Voltage of 110 kV, a current of 90 μA and a focal spot size of 7 μm. The X-ray beam was filtered by a 0.1 mm-thick copper filter. A set of 1440 radiographs (projections) of the xenoliths was recorded over a total scan angle of 360° by a 12-bit, 2400x2400 pixels flat panel detector (Hamamatsu C7942SK-25, pixel size: 50 μm). The virtual axial slices were reconstructed in 32-bit Tiff format, with an isotropic voxel size ranging from 21 to 30 μm (see Table 2) and using the commercial software DigiXCT (DIGISENS, France).

Step B used cone-beam polychromatic X-ray imaging measurements performed at the TomoLab station of the Elettra synchrotron facility in Trieste, Italy (Mancini et al. 2007; Polacci et al. 2009). The instrument is equipped with a sealed microfocus X-ray source (Hamamatsu L9181) with a minimum focal spot size of 5 μm and can operate both in absorption and phase-contrast modes (Wilkins et al. 1996; Zandomeneghi et al. 2010). A set of 2400 projections was acquired for every sample, over a total scan angle of 360°, by a 12-bit, water-cooled, 4008 x 2672 pixels CCD camera (Photonic Science XDI-VHR, UK) with a gadolinium oxysulfide scintillator screen coupled to a fiber-optic taper. A 2 x 2 binning was applied to the detector pixels to improve the signal-to-noise ratio. Scanning conditions were: Voltage = 130 kV, current = 61 μA, filter = 1.5 mm-thick Al foil, exposure time per projection = 6.5 s. The tomographic reconstruction was made by the free software Nrecon 1.7 (Bruker, USA) in 16-bit Tiff format with an isotropic voxel size ranging between 6.25 and 17.5 μm, (see Table 2). In this step, we focused on selected sub-volumes of interest (VOIs) inside the xenoliths.

Both software tools used for tomographic reconstruction in steps A and B are based on the FDK algorithm (Feldkamp et al. 1984) for the cone beam geometry of the X-ray beam.

Steps C and D involved the use of synchrotron radiation microtomography at the SYRMEP beamline of Elettra (Tromba et al. 2010). Cylindrical samples of 4 mm in diameter were drilled or cut from the sub-volumes analyzed in Step B. At SYRMEP, a bending magnet source delivers a nearly-parallel, laminar section X-ray beam with a maximum area of 160 x 6 $mm^2$, at a distance of ca. 24 m from the source. The beamline is equipped with a Si (111) double crystal monochromator allowing work at an energy between 8.3 and 40 keV. It is also possible to operate in filtered white-beam (‘pink’) mode. Our experiment was performed in the ‘pink’ modality using as filters a 1.5 mm-thick Si plate plus a 1.0 mm-thick Al one, giving a mean energy of the X-ray spectrum of ca. 27 keV. For each scan, 1440 projections were acquired over a total scan angle of 180° during continuous sample rotation. The detector used is a 16-bit, water-cooled, 2048x2048 pixels sCMOS macroscope camera (Hamamatsu C13440-20CU) lens-coupled to a 17 μm-thick GGG:Eu scintillator screen. The μ-CT experiments were carried out in propagation-based phase-contrast mode (Cloetens et al. 1997; Baker et al. 2012a; Polacci et al. 2015) setting a sample-to-detector distance of 150 mm. Steps C and D involved the acquisition of images with an effective pixel size of 2.5 and 0.9 um, respectively. In step C we analyzed samples in their entire diameter, in step D we imaged sub-volumes of interest. The tomographic reconstruction was carried out by using the Syrmep Tomo Project (STP) 3.1 software suite developed at Elettra (Brun et al. 2015) based on the filtered back-projection algorithm (Herman 1980) and powered by the ASTRA Toolbox (van Aarle et al. 2015). Before tomographic reconstruction, a single-distance phase-retrieval algorithm (Paganin et al. 2002) was applied to the projection images. The d/β parameter (ratio between the departure from the unit of the real part and the imaginary part of the refraction index of the investigated sample material) was optimized for the different samples. This optimization was done on an ad-hoc base to increase the visibility of the phases of interest.

Every sample was cut to obtain thin sections of about 30 μm with polished surfaces. Thin-section preparation was performed at the University of Padua, Department of Geosciences. 2D textural analysis of samples was carried out in the University of Trieste, Department of Mathematics and Geosciences with a Leitz Wetzlar optical microscope equipped with 5 lenses of, respectively, $2.5/_{0.08}$X, $6.3/_{0.20}$X, $16/_{0.43}$X, $25/_{0.55}$X, $40/_{0.70}$X magnification and a Canon EOS 700D camera. All the images of thin sections were processed with the open-source software Gimp (Gnu Image Manipulation Program).

For sample MG10x the μ-CT protocol described in step A has been applied to the whole xenolith before cutting it into thin sections as the preliminary 3D imaging analysis showed a spinel layering. For samples Bi4 and FN38, thin-section petrographic analyses and μ-CT experiments were performed on two different fragments of the same xenoliths. No oriented structures have been observed for these two samples.

| | **Voxel sizes (µm)** | | | |
|---|---|---|---|---|
| **Sample:** | **MLab laboratory** | **TomoLab laboratory** | **SYRMEP beamline** | |
| | *step A* | *step B* | *step C* | *step D* |
| MG10x | 30 | 10 | 2.5 | |
| Bi4 | 21 | 6.25 | 2.5 | 0.9 |
| FN38 | 23.3 | 6.7 | 2.5 | 0.9 |

*Table 2: Voxel size for the different microtomographic data reconstructed for the mantle xenoliths in this study.*

## 2.3 3D image processing and analysis

One of the important steps in μ-CT data processing and analysis is the definition of a representative elementary volume (REV) that averages all the variable properties of the sample. Considering mantle xenoliths, we believe the multi-scale approach presented here is the most appropriate way to analyze and define a REV. At every 3D imaging step, we defined a volume of interest (VOI) as large as possible, verifying that in the subsequent step, we analyzed a part of the sample still representative of all its properties.

For all μ-CT setups employed, the virtual sections (both raw and processed data) were visualized using the open-source software ImageJ (Schneider et al. 2012) while the 3D visualization, through isosurface or volume rendering tools, was performed by the Dragonfly software (ORS, Canada), version 2020.2 for Windows, using a non-commercial license for academic use. Image processing and analysis were also performed using the Dragonfly software.

The first step of data processing was 3D image segmentation using the corresponding panel integrated into the software, applying to the grayscale an automatic threshold or a locally adaptive threshold in more complex cases. Sometimes the complexity of data or a too-low-density contrast required a semi-automatic segmentation coupled with interpolation operations (i.e. interpolating operations made every 5 to 10 slices to the entire slices dataset, repeating the process for each dimension). After segmentation, a cleaning procedure was applied to exclude from the segmented region of interest (ROI) eventual small defects, undesired and/or unphysical objects as outliers or noise. Segmentation and cleaning were based not only on morphological operations (erosion and dilation of the selected volume) but also on topological properties (connectivity, elongation, voxel count, etc). For each ROI, several structural, morphological and textural parameters can be computed. For example, if the ROI is composed of disconnected volumes, as in the case of different spinel crystals, the connected component analysis allows separation, labelling and quantification of several parameters for each element. In Table 3, we list the parameters extracted from the 3D data process and considered the most useful for this study. The calculation of these parameters is particularly useful when considering mineral phases, as it allows us to define the origin of a crystal, and also to understand the nature and formation processes of pores and vesicles.

In the case of volumes characterized by highly interconnected features, applying a skeletonization approach, by using the Dragonfly software, it is possible to describe and analyze the complexity of interconnected spaces. Throughout this analysis, we determined the number of vertices and edges of the skeletal model, deriving edges/vertices ratios, the Euclidean length of edges and connectivity density (CD) of analyzed objects. The connectivity density, in particular, gives an idea of skeleton complexity and connectivity, and is given by a scalar value representing the number of redundant connections normalized to the total analyzed volume V (Zandomeneghi et al. 2010) and computed as CD = [1 – (n-b)]/V, being n the number of vertices and b the number of edges. Highly connected volumes should have very low and negative values of connectivity density. On the other hand, high positive values of connectivity density indicate volumes not connected.

| Parameter | Notes |
|---|---|
| Voxel count | Total number of voxels in each labelled object. |
| Volume | Volume occupied by each labelled object, that is, the amount of space inside of the object. |
| Surface | The surface area of each labelled object, that is, it refers to the outside area of the object. |
| Volume/Surface | Calculated volume-to-surface area ratio. |
| Phi | The angle from the X axis of the projection on the XZ plane of the orientation. |
| Theta | The angle from the X axis of the projection on the XY plane of the orientation. |
| Aspect ratio | Proportional relationship between the smallest eigenvalue and the largest for the inertia eigenvectors. A perfect cube or sphere would have an aspect ratio of 1.0, while a square or circle would have an aspect ratio of 0.5. |
| Mean intensity | Mean value of all voxels found for each object. |
| Elongation | Ratio of the minimum orthogonal Feret diameter to the maximum Feret diameter. |
| Entropy | Histogram-based descriptor In image processing entropy might be used to classify textures; a certain texture might have a certain entropy as certain patterns repeat themselves in approximately certain ways. A component with low entropy is more homogenous than a component with high entropy. |

*Table 3: Main connected components analysis parameters extracted from the 3D data processing. A more complete description of these parameters can be found at www.theobjects.com/dragonfly.*

The petrographic characterization of thin sections allowed identification of up to eight different phases: olivine, clinopyroxene, orthopyroxene, spinel, glass, sulfide, serpentine and fractures/voids. The segmentation of μ-CT data was hence performed, bearing in mind the possible presence of these phases, and by cross-checking the data with the results of petrography on thin sections. Given the low attenuation contrast between olivine, clino- and orthopyroxene, these minerals were segmented as an individual phase called "silicates". Any phase showing grey levels higher than spinel was identified as sulfide.

# 3 Results

## 3.1 Xenolith MG10x (Mandalgovi, Mongolia)

Considering the thin section observations and following the classification of Harte (1977), Mongolian mantle xenolith MG10x (Fig.1A) is a granuloblastic spinel-lherzolite. It shows abundant three-grain junctions with ~120° between boundaries, which are mainly straight, sometimes curving, and with abundant serpentine between crystals (Fig.1B). Fluid inclusion trails are diffused inside silicates (Fig.1B), likely reflecting the entrapment of fluids during the annealing of old fractures. Inside the larger fluid inclusions (ca. 30 μm), it is possible to recognize a small shrinkage (5 μm) of bubbles and opaque phases and in many cases the longer and thinner ones pinch off to form separate rounded inclusions. Many inclusions have negative-crystal shapes. Olivines have kink-banding and, in one crystal, an inclusion of sub-rounded spinel. Pyroxenes have no exsolution lamellae except in one crystal of clinopyroxene. Nearly all the clinopyroxenes display a thin spongy rim. Spinels appear as holly-leaf in shape and brown in color (Fig.1A). Sporadically some sulfide minerals are present (Fig.1C), usually rounded in shape, apparently associated with the alteration in serpentine but, in some cases, they are included in olivine and pyroxenes.

Tomographic data obtained at a voxel size of 30 μm (step A) show that sample MG10x has a total volume of $1.27 \cdot 10^{13}$ $\mu m^3$. 3D images segmentation produced three distinct phases: silicates (99.000 vol%), spinel (0.998 vol%) and sulfide (0.002 vol%). Connected component analysis shows that sulfides differ from spinels for higher mean intensity and aspect ratio (Supplementary Table 1 and Supplementary Figure 1). Spinel forms groups of crystals that are mostly aligned along two distinct layers (Fig.2A). Note that such layers were not detectable by observing the xenolith in hand sample. Spinel is always vermicular in shape and tends to form interconnected volumes within each layer. To quantify the possible interconnection of spinels in the layers we performed a skeleton analysis on this ROI (Table 4).

Small sulfide grains occur throughout the analyzed volume. Their distribution appears not to be associated with spinel layering. At this resolution, they appear rounded in shape.

The sub-volume analyzed at a voxel size of 10 μm (step B) has a total volume of $2.46 \cdot 10^{12}$ $\mu m^3$. It was drilled off the original sample perpendicularly to the spinel layering (see Fig.2B) to detect small-scale (< 300 μm) textural or mineralogical variations associated with the layering. Segmented phases were the same as at step A and no textural or mineralogical variations were detected. Increasing the resolution allows us to better define the interconnection of spinel crystals inside layers, which is poor, as shown in Table 4 and Supplementary Figure 2. Sulfides appear sub-rounded in shape, with volumes of individual grains ranging from $1.30 \cdot 10^4$ $\mu m^3$ to $6.16 \cdot 10^6$ $\mu m^3$ (with more than 50% of the volumes being below $6.00 \cdot 10^5$ $\mu m^3$).

The sub-volume analyzed at a voxel size of 2.5 μm (step C), which was in turn extracted from the sub-volume analysis at step B, has a volume of $1.13 \cdot 10^{11}$ $\mu m^3$. At these conditions segmenting the spinel is challenging as it has a similar refraction index to the silicates. Working with segmentation in a reduced volume, avoiding the edge of the imaged sample, is useful to decrease noise. The higher spatial and contrast resolution at this step allowed us to better define the shape of the sulfide grains (Fig.2C), which are sub-rounded to skeletal-like, completely amorphous or interstitial to other phases grains. In addition, it was possible to segment serpentine (Fig.3), which occurs as low-intensity thin films, 10 to 30 μm thick, surrounding the silicates of the xenolith.

| Sample | Step | Phase | Volume (mm$^3$) | Surface (mm$^2$) | Feret diameter (mm) Min | Feret diameter (mm) Max | Edges/ Vertices ratio | Connectivity density (mm$^{-3}$) |
|---|---|---|---|---|---|---|---|---|
| MG10x | A | Spinel layers | 118.30 | 1’067.95 | 20.06 | 43.40 | 0.98 | -2.87 |
| MG10x | B | Spinel layers | 53.17 | 892.56 | 12.40 | 19.11 | 1.05 | 124.23 |

*Table 4: Skeleton analysis results summarized for spinels of sample MG10x*

## 3.2 Xenolith Bi4 (Bou-Ibalrhatene, Morocco)

Based on 2D thin-section petrographic observation, sample Bi4 (Fig.4) is a protogranular spinel-lherzolite with an average grain size of 2.0 mm (Mercier and Nicholas 1975). Grain boundaries are mostly curving or irregular. Occasionally, three-grain junctions with ~120° are present, particularly among the smaller crystals. There are many fluid inclusion trails, usually multiphase, along fractures of both olivine and pyroxenes. Microcrystals, smaller than 15 μm in diameter with euhedral habit, are recognized in fluid inclusions. In many cases, smaller secondary inclusions radiate from larger ones. There are many blebs with variable sizes (0.5–3.0 mm) and complex shapes, usually associated with spinel (Figs. 4B and C). Inside these blebs, there are microcrystals of olivine, pyroxene, opaque phases and some voids, generally sub-rounded in shape. Grains in contact with blebs occasionally display the growth of newly formed magmatic crystals.

Mineral grains display evidence of deformation, particularly by the presence of strongly undulating extinction and kink banding in olivine and sporadically curved cleavage in pyroxene. Olivine displays occasionally inclusions of sub-rounded spinel. Pyroxenes have no spongy rims, and no exsolution lamellae except for one orthopyroxene and one clinopyroxene in the thin section. In addition, clinopyroxenes commonly show some elongated elliptic and brownish inclusions. Spinel forms holly-leaf crystals and is always associated with microcrystalline blebs, except for the tiny subhedral spinel included in olivine or located at the junction between silicates. Unidentifiable opaque phases, possibly sulfide, are present within blebs and occasionally as interstitial phases.

Tomographic data acquired at a voxel size of 21 μm (step A) show that sample Bi4 has a total volume of $3.43 \cdot 10^{12}$ μm$^3$. Segmentation produced three distinct phases (Fig.5A): silicates (97.900 vol%), spinel (1.491 vol%), high-density phases (HDP; 0.017 vol%) and voids (0.592 vol%). Connected components analysis for high-intensity volumes (spinels and HDP) and voids are given in Supplementary Table 1. As underlined for sample MG10x, statistical analyses allow for discrimination between spinel and HDP (Supplementary Figure 3). Spinel is arranged both in small anhedral crystalline aggregates with individual volumes ranging from $9.26\cdot10^3$ μm$^3$ to $2.00\cdot10^9$ μm$^3$ and bigger vermicular clusters (Fig.5A) with volumes ranging from $5.73\cdot10^9$ μm$^3$ to $1.76\cdot10^{10}$ μm$^3$. High-density phases are rounded and smaller concerning spinel and appear to be spread all over the xenolith, with a particular concentration at the contact between xenolith and host basalt (Fig.5A). The xenolith has a considerable volume of voids, sub-rounded in shape, that appear to be concentrated on the surface of the large spinel clusters (Fig.5A). The μ-CT images allowed identification of several fractures (from 90 to 350 μm in width), particularly a large one bisecting the xenolith.

The analysis of μ-CT data with a voxel size of 6.25 μm (step B) focused on the upper portion of xenolith Bi4 (Fig.5C), having a total volume of $2.54\cdot10^{11}$ μm$^3$. Segmented phases are the same as in step A. Spinels form a large cluster of $1.16\cdot10^{10}$ μm$^3$, with several crystals of intermediate dimensions and many smaller (average volume of $1.00\cdot10^9$ μm$^3$). Spinel is always surrounded by blebs of small neoblasts, euhedral in shape, with low-density material in between. The large spinel cluster displays the presence of several inclusions with low brightness (Fig.5B) that are not in contact with the surface of the spinel, which suggests they might be primary melt inclusions. Larger ones seem to be composed of the same aggregate as the blebs, while smaller inclusions are usually glassy, sometimes with a gas bubble inside. Voids are arranged in three patterns: surrounding the large spinel cluster; dispersed around the small spinel crystals; and aligned along the surfaces, hinting at the existence of several possible fractures. Some voids appear isolated (0.66 vol%, considering the sub-volume in step B) while others appear interconnected within the limits of our imaged sample (35.2 vol%).

The sub-volume analyzed at step C ($6.07\cdot10^{10}$ μm$^{3;}$ voxel size: 2.5 μm; Fig.5D) has been extracted from the sub-volume analyzed at step B. It shows approximately $2.20\cdot10^9$ μm$^3$ of spinel, which was manually segmented. High-density materials occupy a volume of $7.00\cdot10^7$ μm$^3$ and, at this resolution, it was possible to better define their texture. Larger volumes are present at the top of the sample (Fig.5D), aligned with the surface at the edge of the xenolith; there are several small, rounded crystals scattered inside blebs of silicate neoblasts surrounding spinel. There are also some small anhedral and elongated phases inside fractures (Fig.5D), these are the brightest when considering the absorption of high-density material (Fig.5E). Fractures are visible inside all the analyzed volume and are sometimes connected with the blebs surrounding spinel. The material composing blebs and filling the fractures seems to be the same (Fig.5E), with the difference that larger euhedral neoblast are preferentially inside blebs, which are wider. The area between neoblasts is filled by voids and by a low-density material, similar in adsorption concerning silicates (it was not possible to segment it at the current stage) which is also the main phase present inside fractures. Voids are therefore present both in blebs surrounding spinel and in fractures, showing a sub-rounded bubble-like shape. The total volume of voids inside the analyzed sample is $3.96 \cdot 10^9$ $\mu m^3$ and they are all isolated concerning the edges of the xenolith. That means void bubbles are not connected nor to the exterior of the xenolith. The top of the xenolith was imaged at a higher resolution, with a voxel size of 0.9 μm (step D), to better characterize the high-density material that here appears as more concentrated (Fig.5F).

## 3.3 Xenolith FN38 (Fernando de Noronha, Brazil)

Optical petrography defines sample FN38 (Fig. 6A) as protogranular lherzolite with some large crystals of olivine. Grain boundaries are mainly irregular, sporadically straight and showing some triple junctions. Olivine has kink bands, particularly in the larger crystals, while clinopyroxene has a spongy texture. The main characteristic of this xenolith is the presence of extended patches, embedded in the coarse matrix, made by glass and subequal neoblasts crystallized inside (Figs. 6B and C). Inside these patches, there are some vesicles filled with zeolites. In the thin section, spinel is always inside these patches, forming small euhedral crystals. There are some smaller glassy pockets, preferentially developed at the junction of grains. Neoblasts in the glassy patches commonly have euhedral shape. These are mainly small euhedral olivine, spongy aggregates of clinopyroxene, euhedral spinel crystals and rare plagioclase, in one case showing zoning. The bigger patches have little glass and olivine crystals inside, which are irregular in shape and display no reaction rim. On the contrary, smaller patches are characterized by the absence of olivine crystals and by the presence of abundant glass.

Considering the computed microtomography, step A was carried out with a voxel size of 23.3 μm (Fig. 7A); the total analyzed volume is $6.02 \cdot 10^{12}$ $\mu m^3$. Segmented phases are silicates (98.500 vol%), glass (1.494 vol%) and spinel (0.006 vol%). Connected components analysis of glasses and spinels are given in Supplementary Table 1. Spinel shows a higher absorption (given the same instrumental conditions and pre-processing operations) concerning the MG10x and Bi4 spinel and is arranged in small ($1.64 \cdot 10^7$ $\mu m^3$) crystals aggregates, with no evidence of large clusters. The glass phase is abundant and occurs surrounding spinel. Glass forms either small, isolated patches or elongated pockets, sometimes interconnected among them and in contact with the surface of the analyzed volume (note that this does not correspond to the contact between xenolith and host lava). At this spatial resolution, half of the total glass volume (0.756 vol%) appears as pockets that are isolated from the surface of the investigated sample. To better define the interconnectivity of the glass we performed a skeleton analysis on this ROI. Results show high interconnectivity and are summarized in table 5 and Supplementary Figure 4.

Step B (voxel size: 6.7 µm) focused on the central part of sample FN38, analyzing a total volume of $8.00 \cdot 10^{11}$ µm$^3$. Segmented phases are the same as in step A (Fig. 7B). No further textural details were noted for spinel (see the slice in Fig. 7B). Also, at this spatial resolution, a portion of the glass (1.005 vol%, relative to total volume of the sample) appear not connected to the edges of the analyzed volume.

Step C focused on the inner part of the volume analyzed at step B, imaging a total volume of $9.64 \cdot 10^{10}$ µm$^3$. The main improvement is the imaging of microlites of spinel inside the glassy patches (Fig.7C) and some vesicles filled with a material similar in density to the silicic glass (possibly zeolites), which were undetectable at lower resolutions and visible only in the thin section.

A selected volume of interest was imaged with a voxel size of 0.9 µm (step D). Here it was possible to better characterize the low-density volumes. There are not only glass patches but also tiny films of glass occupying the intercrystalline space (Fig.7D).

| **Sample** | **Step** | **Phase** | **Volume** | **Surface** | **Feret diameter (mm)** | | **Edges/ Vertices ratio** | **Connectivity density** |
|---|---|---|---|---|---|---|---|---|
| | | | **(mm$^3$)** | **(mm$^2$)** | **Min** | **Max** | | **(mm$^{-3}$)** |
| FN38 | A | Glass | 91.19 | 2’071.96 | 16.25 | 52.62 | 0.92 | -72.30 |
| FN38 | B | Glass | 8.04 | 781.08 | 8.33 | 15.10 | 0.95 | -3499.27 |

*Table 5: Skeleton analysis results summarized for glasses of sample FN38.*

# 4 Discussions

All xenoliths were brought to the surface via OIB-like alkaline intraplate magmatism. The Mongolian (MG10x) and Moroccan (Bi4) samples in a continental one, while Fernando de Noronha’s sample (FN38) is from a true OIB. The Mongolian xenolith represents a piece of the lithosphere in a mobile belt zone, Bi4 a xenolith from a pericratonic area while FN38 comes from the upper mantle beneath the oceanic crust. This implies that the depth of sampling varies for the three xenoliths.

## 4.1 Spinel morphology

In mantle xenoliths, spinel can occur with various morphologies, from vermicular to skeletal or even euhedral crystals (Matsumoto and Arai 2001). According to Mercier and Nicolas (1975), in protogranular peridotites spinels are considered as an exsolution product from enstatite and they recrystallize to an interstitial or mosaic shape. In xenoliths with a porphyroclastic texture, which are considered the product of the deformation of protogranular peridotites, spinel recrystallizes to elongated holly-leaf-shaped grains. In equigranular textures, polygonal spinels may occur between the other crystals. Pike and Schwarzman (1977) considered the presence of euhedral spinel in or between silicates as indicative of a so-called igneous xenolith.

Pyrometamorphic textures are caused by the solidification of local partial melts within the rocks. Here, tiny quench crystals of euhedral oxides can be found (Pike and Schwarzman 1977). In xenoliths that have undergone limited recrystallization or are in early stages of polygonization, spinels are small, disseminated, forming holly-leaf interstitial grains because silicates are reduced in size by polygonization and mechanical breakdown (Pike and Schwarzman 1977). In foliated and equigranular mosaic textures, spinel is interstitial in clumps or strings parallel to the foliation (Pike and Schwarzman 1977). Samples MG10x and Bi4 show anhedral spinel (Fig. 1B and 4C), which is termed holly leaf (Mercier 1975) and is characterized by the presence of appendices that extend into the silicate matrix surrounding the spinel.

Our μ-CT results show how the morphology and texture of spinel grains are fully understandable only through a 3D reconstruction. Consider for example the thin section of sample Bi4 (Fig. 4) where spinel appears with a classical holly leaf shape, it is surrounded by microcrystalline blebs and shows no visible inclusions. μ-CT shows that in this sample the spinel is present in two main forms (Fig. 5A): big clusters with high surface/volume ratios and small sub-rounded crystals. The first case is always surrounded by voids, while it is difficult to evaluate if the same is true for the second spinel occurrence. Furthermore, at higher resolution (step B and following, Figs. 5C and 5D) the large spinel cluster appears rich in several inclusions, which were not detected in the thin section under the optical microscope. These inclusions are always rounded in shape and are filled with the phases with the same contrast of those present in the bleb that surround the spinel (see Chapter 4.4).

In sample FN38 the 3D model underlined the presence of aggregates of spinel crystals that in the thin section may be confused with whole spinel grains. Furthermore, the spinel of FN38 is highly absorbing compared to the other two xenoliths, which probably reflects different compositions. In sample FN38 there is no holly-leaf spinel with high surface/volume ratios, and the few crystals present appear to be formed by aggregates of smaller ones (Fig.7A), with high absorbance. Increasing the resolution to 2.5 μm of voxel size (step C, Fig.7C), it is possible to notice another kind of spinel, scattered in the glass and smaller in size. This is the spinel we observed in thin section, crystallized inside glassy patches.

For this textural feature however, the resolution of the μ-CT analysis plays a fundamental role, as at voxel sizes higher than 6.25 μm for sample Bi4 and 2.5 μm for the xenolith FN38 the texture of spinel was not fully characterizable.

## 4.2 Spinel layering

Spinel layering has been investigated in sample MG10x and it is a clear example of how a traditional thin section may hamper an appropriate interpretation of the xenolith. A bigger problem is the random sectioning plane of a thin section, and even with a targeted thin section (Fig.1), it is difficult (if not impossible) to find all the information that is instead clearly evident with the 3D model obtained with computed microtomography.

The spinel layering is poorly defined in thin sections even in a targeted section, but identifiable in the 3D μ-CT model. Even in lower resolutions, it is possible to recognize at least two different spinel layers crossing the sample and suggesting a fragile zone - rather than ductile - as the source of this mantle xenolith.

Moreover, in optical microscopy, spinel appears as classical mantle spinel with a holly-leaf texture. Even its absorption in the μ-CT slices suggests a composition similar to that of restitic spinel, as in sample Bi4. However, given its arrangement in layers, it is more appropriate to classify this kind of spinel as magmatic, crystallized directly from a melt that percolated the mantle. This speculation is particularly plausible for the MG10x sample, as the geodynamic setting of the region suggests the presence of a fragile zone in the mantle at the depth in which the xenolith was sampled, and metasomatic melts may percolate along fractures, leading to the formation of spinel layers. This kind of layering is discussed in the literature, for both spinel and other mineral phases, like the example of the Balmuccia peridotite, Italy, showing massive monomineralic spinel layers 10 cm thick (Mazzucchelli et al. 2009), or the websteritic veins in the Lherz Massif (Le Roux et al. 2007), as well as discordant dyke-like chromitite layers in dunite from northern Oman ophiolite (Arai and Miura 2016). However, it is difficult to find studies that describe small-scale layering, thus although the processes may be similar, additional studies are necessary. Considering how difficult it is to identify this textural feature in thin section observation, it is likely to have been overlook in many studies.

Note that these textural interpretations were possible only through the 3D model obtained by μ-CT analysis. With this xenolith, which shows a homogeneous coarse-grained texture, even low-resolution imaging (step A) may be sufficient for a first textural 3D study.

## 4.3 Sulfides

In samples MG10x and Bi4, there are some phases with higher attenuation concerning the spinel grains that were identified as sulfides in optical microscopy. According to the literature, their presence may be correlated to the texture of mantle xenoliths. Szabó and Bodnar (1995), for example, indicate that the distribution of sulfides in the upper mantle is linked to deformation and recrystallization processes, therefore a 3D analysis may be fundamental in understanding the texture and distribution of sulfides. Some authors, such as Wang et al. (2020), tentatively described in three dimensions the mechanism that led to the formation of sulfides inside partially melted peridotite, but they worked with synthetic samples.

In the Mongolian sample MG10x, sulfides are homogenously disseminated into the xenolith, with no apparent spatial relationships with spinel layering. This is confirmed by phi and theta values in the connected component analysis (see Supplementary Table 1), as these variables indicate the orientation of the segmented volumes, similar values mean a similar orientation (a tabular texture for example), and different values mean scattered volumes. Because of the small size and very low abundance of sulfides, this feature cannot be identified in thin section. Moreover, accurately modelling the morphology of these sulfides was possible only through synchrotron radiation-based tomography (Fig. 2C). The crystallization of sulfides is not concomitant with the formation of the spinel or, however, independent from the event that led to the crystallization of spinel. We speculate that considering the distribution of these high-density sulfides, the percolation of small-volume melts in inter-grain spaces may be responsible for their deposition (Wang et al. 2020 and reference therein).

Regarding sample Bi4, there are high-density volumes visible in steps A and B, which appear randomly scattered inside the volume and are not affected by the presence of spinel clusters. At 2.5 μm of voxel size, it is possible to recognize how high-density phases are present only in the percolating melt, sometimes even in the blebs surrounding spinel but preferentially inside fractures. This may suggest an in-situ sulfide liquid immiscibility that led to the precipitation of this kind of elongated sulfide in melt-filled cracks (Fig. 5D and 5E) as proposed by Lorand (1991). We focused a scan with a higher resolution of 0.9 microns (step D, Fig. 5F) on the top of our sample, discovering this was probably a fracture where the xenolith broke. Here we have the bigger volumes with high density and they appear particularly similar to SEM backscatter electron images of sulfide (Hughes et al. 2016).

## 4.4 Glass, voids, fractures

Glasses in xenoliths may represent reaction products between mantle xenoliths and migrating small-volume melts percolating the mantle, which contribute to mantle heterogeneity and metasomatism (e.g., Coltorti et al. 2000; Fialin et al. 2011; Miller et al. 2012; Lahmer 2018), or may be solidified products of in situ melting (Yaxley and Kamenetsky 1999). Despite the importance of such phenomena, the 3D distribution of glasses and gas vesicles inside xenoliths has only been recently studied (Patkó et al. 2020; Casetta et al. 2022).

The Moroccan sample Bi4 shows microcrystalline blebs around spinel in thin section, that are not inter-connected, and sometimes show a glassy film between phases. μ-CT data show no evidence of these blebs using a resolution of 21 μm (step A), probably because of the similar densities of the different silicates, which result in small phase contrast in the acquired data. What is clear from observing this 3D model (Fig. 5A) is the presence of several voids and some fractures that were resolvable at resolutions of 6.25 and 2.5 μm (steps B and C). First, the blebs surrounding spinel, which are not visible at a lower resolution, appear at 6.25 μm and are quite clear at 2.5 μm. Second, some of the microcrystalline blebs are present inside larger spinel grains and show no connections to their exteriors. These are inclusions characterized by the presence of only glass and gas bubbles, preserved inside the spinel. This is another advantage of computed microtomography, i.e., identifing inclusions in both transparent and opaque minerals and verify whether they are connected with the exterior of the host. In the case of our sample, these observations might indicate that the spinels crystallized from the melts that are now represented by the multi-phase blebs. A combination of these data with compositional analyses is needed to confirm such a hypothesis and would provide new constraints on the formations of spinels in mantle peridotites.

Fracture analysis and interpretation are also improved with higher-resolution imaging. At 6.25 μm of voxel size, every fracture may be well characterized, and it is noted that they are filled with the same material that forms the blebs around spinel. This evidence underlines how blebs are not isolated but connected with fractures and thus the formation of blebs may be related to the percolation of melts inside the xenolith, which is probably driven by the prior formation of fractures. Moreover, this melt solidified at sufficiently low pressures to allow degassing, as testified by the presence of several vesicles. Voids are always sub-rounded in shape and present in blebs as in fractures (see Figs. 5D and 5E).

The particularity of sample FN38 is the widespread presence of glassy patches, in which there are newly crystallized phases and some voids filled by zeolites. This is evidence of melts percolating the mantle or at least the xenolith, though it is unclear considering the two-dimensional section if the glassy patches are isolated or represent channels extending through the xenolith. In the three-dimensional model, obtained with μ-CT at 23.33 μm of voxel size (Fig. 7A), it is noted that glass is scattered all around the sample and, in contrast to the blebs of sample Bi4, its presence seems to be independent of the spinel. Interconnection may be more evident considering connectivity density in the skeleton analysis (Table 5); this allows to confirm this melt is not (or not only) the product of the partial melting of some crystals but represent a liquid phase that permeated the xenolith. When considering smaller voxel sizes, such as 6.7 μm, the connection between glassy patches appears clearer and thus volumetric considerations are more robust. Comparing all the resolutions used in the acquisition of μ-CT scans, glassy patches appear as largely diffuse and highly interconnected (through both large channels and small intergranular spaces), indicating that melts were percolating extensively in the mantle section sampled by the xenoliths.

## 4.5 Modal proportions of spinel

It is common use in petrography to estimate the volumetric percentage of a mineral over a 3D sample by using point counting or image analyses on a single 2D thin section. However, if the sample is anisotropic, applying this procedure to sections that have been randomly cut from the sample may add unknown errors in the estimate. To quantitatively evaluate such errors, we simulated the acquisition of several 2D slices: this allows us to compare the areal percentage estimated from each 2D thin section with the actual value calculated from the entire volume.

We started from the labelled 3D model obtained with the lower resolutions (step A) and we took 50,000 random slices over the three axes. To better simulate the real slicing process, the only constrain applied to this random process was that the obtained slice must have an area at least equal to the slice taken orthogonal to the longest axis. This constraint is introduced to avoid the algorithm taking into account unrealistic slices, e.g. a thin section that takes only a small portion of the whole sample.

By doing this, we can simulate the estimation of the percentage of spinel that would arise from each 2D thin section. Results may be seen in Fig. 8 for the three studied xenoliths.

Assuming a normal distribution of the samples we fit the estimated volumetric percentage of spinel with:

$$f(x) = \alpha * e^{-\left(\frac{(x-\mu)}{2\sigma^2}\right)^2}$$

Where α is $\frac{1}{\sqrt{2\pi\sigma^2}}$, $\mu$ is the mean value and $\sigma$ is the standard deviation (std).

In Table 6 the parameters of the gaussian fit of the distribution are presented.

| Sample | Real Mean | $\mu$ | $\sigma$ | R-squared |
|---|---|---|---|---|
| MG10x | 0.9265 | 0.8663 | 0.5199 | 0.9912 |
| Bi4 | 1.4143 | 0.9543 | 1.653 | 0.99 |
| FN38 | 0.0298 | - | - | - |

*Table 6: Resuming data of the thin section simulation and relative parameters.*

Sample MG10X present a distribution centered in 0.87 vol% with a standard deviation of 0.52 vol%: there are outliers in the range [2.00–3.00 vol%] that may be due to the layered distribution of spinel in the sample.

Sample Bi4 shows a trend similar to MG10x, but it has a higher range of variability with a mean of 0.95 vol% with a standard deviation of 1.65 vol%. The higher standard deviation should be due to the cluster distribution of spinel, which increases the probability of incorrect identification of the right value.

While MG10X and Bi4 fit well in a Gaussian distribution, FN38 does not. This may be due to the very low abundance of the mineral in the sample and its uniform distribution.

According to the empirical rule (Pukelsheim 1994):

$$Pr(\mu - 1\sigma \leq X \leq \mu + 1\sigma) \approx 68.27\%$$

This can be used to determine the range of modal estimates obtainable by using point counting on a random thin section. For xenolith MG10x, which has a spinel mode of 0.93 vol%, there is a probability of 68.27% to estimate a mode between 0.35 vol% and 1.39 vol% using point counting on such thin section. For xenolith Bi4, which has a spinel mode of 1.41 vol%, the range is between 0.00 and 2.60 vol%. This clearly shows that point counting on a randomly cut thin section in such type of xenoliths can produce misleading results in terms of abundance of minor and accessory phases.

# 5 Implications

We applied multi-modal X-ray microtomographic imaging to characterize at different scales the textural properties of three mantle xenoliths collected from different geodynamic settings. The extracted volumetric models allow to define the texture of the samples with completeness and detail not achievable with classical 2D thin sections analysis. The multi-scale approach applied to a variety of textures allows development of a series of recommendations for future petrological studies of mantle xenoliths through X-ray micro-CT:

- If the goal of the study is to verify possible spinel layering, low-resolution X-ray μ-CT (as our step A) may be sufficient and might allow characterization of the whole xenolith, which typically has a size in the range of 1–10 cm.
- Characterizing spinel morphology and internal texture requires higher resolutions, 0.9 to 1.5 μm of voxel size (steps C and D). This allows identification of possible inclusions, which are important for interpreting prevailing conditions during spinel formation. The lower resolution of steps A and B may lead to misinterpretation of textures, as was the case with the small spinel crystals of FN38, visible only at 2.5 and 0.9 μm of voxel size.
- The presence and distribution of sulfides were estimated through thin-section observations, but the modal abundance, distribution and textures were quantified only through μ-CT. In the volumetric analysis, the distribution of high-density minerals is easy to achieve even at low resolutions (step A), due to their high attenuation coefficient. For the texture, because of the small size of these phases and the high absorbance, a small voxel size (steps C and D) is necessary to properly characterize the shape. As shown in Figs .2C and 5F we obtained the best results with a voxel size of 2.5 μm for sample MG10x and 0.9 μm for sample Bi4. Moreover, considering the very low abundance of sulfides and platinoids inside mantle samples, it is worth noting that with a proper 3D reconstruction it may be simpler to target with high precision where to cut the sample for further analysis.
- In the thin section, voids are visible inside microcrystalline blebs and their sub-rounded shape is identifiable. However, only through 3D reconstruction at high resolution (e.g., our steps C and D) is it possible to accurately quantify such voids and even detect those that are inside the fractures of the xenolith.
- Calculation of modal proportion of spinel, and any other phase, inside mantle xenoliths through 2D analysis of randomly cut thin sections should be carefully evaluated. As our simulation demonstrates, if the distribution of a phase is not homogeneous inside the cut volume, the uncertainties of the modal estimates with a classical thin section can increase and even be difficult to quantify.

## Acknowldegments

The authors acknowledge Elettra Sincrotrone Trieste for access to the SYRMEP beamline and TOMOLAB (Proposal No. 20195185) and the staff members for their help in performing the computed microtomography experiment. Lorenzo Furlan and Leonardo Tauro are thanked for the assistance in preparing the samples for this study. The associate editor and two anonymous reviewers are thanked for the valuable inputs that improved the manuscript.

# References

Arai, S., & Miura, M. (2016). Formation and modification of chromitites in the mantle. Lithos, 264, 277-295.

Arzilli, F., Polacci, M., Landi, P., Giordano, D., Baker, D. R., & Mancini, L. (2016). A novel protocol for resolving feldspar crystals in synchrotron X-ray microtomographic images of crystallized natural magmas and synthetic analogs. American Mineralogist, 101(10), 2301-2311.

Bhanot, K. K., Downes, H., Petrone, C. M., & Humphreys-Williams, E. (2017). Textures in spinel peridotite mantle xenoliths using micro-CT scanning: examples from Canary Islands and France. Lithos, 276, 90-102.

Bhanot, K. K., Downes, H., Petrone, C. M., Humphreys-Williams, E., & Clark, B. (2020). Micro-CT investigation of garnet-spinel clusters in mantle peridotite xenoliths. Lithos, 352, 105250.

Baker, D. R., Mancini, L., Polacci, M., Higgins, M. D., Gualda, G. A. R., Hill, R. J., & Rivers, M. L. (2012a). An introduction to the application of X-ray microtomography to the three-dimensional study of igneous rocks. Lithos, 148, 262-276.

Baker, D.R., Brun, F., O'Shaughnessy, C., Mancini, L., Fife, J., Rivers M.L., (2012b). A four dimensional X-ray tomographic microscopy study of bubble growth in basaltic foam, Nature Communications 3, 1135.

Blanks, D. E., Holwell, D. A., Fiorentini, M. L., Moroni, M., Giuliani, A., Tassara, S., ... & Ferrari, E. (2020). Fluxing of mantle carbon as a physical agent for metallogenic fertilization of the crust. Nature communications, 11(1), 1-11.

Brun, F., Accardo, A., Kourousias, G., Dreossi, D., Mancini, L., Tromba, G., Pugliese, R. (2015). Enhanced and Flexible Software Tools for X-ray Computed Tomography at the Italian Synchrotron Radiation Facility Elettra. Fundamenta Informaticae, 141, 233-243.

Carlson, W.D. (2006). Three-dimensional imaging of earth and planetary materials. Earth and Planetary Science Letters, 249, Issues 3–4, 133-147.

Casetta, F., Rizzo, A. L., Faccini, B., Ntaflos, T., Abart, R., Lanzafame, G., ... & Coltorti, M. (2022). CO2 storage in the Antarctica Sub-Continental Lithospheric Mantle as revealed by intra-and inter-granular fluids. Lithos, 416, 106643.

Chanouan, L., Ikenne, M., Gahlan, H.A., Arai, S., Youbi, N. (2017). Petrological char- acteristics of mantle xenoliths from the Azrou-Timahdite quaternary basalts, Middle Atlas, Morocco: a mineral chemistry perspective. J. Afr. Earth Sci. 127, 235–252.

Cloetens P., Pateyron-Salomé, M., Buffière, J.Y., Peix, G., Baruchel, J., Peyrin, F., and Schlenker, M., (1997). Observation of microstructure and damage in materials by phase sensitive radiography and tomography: Journal of Applied Physics 81, 5878–5886.

Cnudde, V., & Boone, M. N. (2013). High-resolution X-ray computed tomography in geosciences: A review of the current technology and applications. Earth-Science Reviews, 123, 1-17.

Coltorti M., Beccaluva L., Bonadiman C., Salvini L. & Siena F. (2000). Glasses in mantle xenoliths as geochemical indicators of metasomatic agents. Earth and Planetary Science Letters 183, 303–320.

Créon, L., Rouchon, V., Youssef, S., Rosenberg, E., Delpech, G., Szabo, C., ... & Guyot, F. (2017). Highly CO2-supersaturated melts in the Pannonian lithospheric mantle–A transient carbon reservoir? Lithos, 286, 519-533.

Feldkamp, L. A., Davis, L. C., & Kress, J. W. (1984). Practical cone-beam algorithm. Journal of the Optical Society of America 1(6), 612-619.

Fialin, M., Wagner, C., & Pascal, M. L. (2011). Iron speciation using electron microprobe techniques: application to glassy melt pockets within a spinel lherzolite xenolith. Mineralogical Magazine, 75(2), 347-362.

Fodor, R. V., Mukasa, S. B., & Sial, A. N. (1998). Isotopic and trace-element indications of lithospheric and asthenospheric components in Tertiary alkalic basalts, northeastern Brazil. Lithos, 43(4), 197-217.

Guy, A., Schulmann, K., Munschy, M., Miehe, J. M., Edel, J. B., Lexa, O., & Fairhead, D. (2014). Geophysical constraints for terrane boundaries in southern Mongolia. Journal of Geophysical Research: Solid Earth, 119(10), 7966-7991.

Guntoro, P. I., Ghorbani, Y., Koch, P. H., & Rosenkranz, J. (2019). X-ray microcomputed tomography (μCT) for mineral characterization: A review of data analysis methods. Minerals, 9(3), 183.

Harte B. (1977) Rock nomenclature with particular relation to deformation and recrystallisation textures in olivine-bearing xenoliths. J. Geology 85, 279–288.

Herman, G. T. (1980): Image reconstruction from projections - the fundamentals of computerized tomography. New York, Academic Press.

Hidas, K., Falus, G., Szabó, C., Szabó, P. J., Kovács, I., & Földes, T. (2007). Geodynamic implications of flattened tabular equigranular textured peridotites from the Bakony-Balaton Highland Volcanic Field (Western Hungary). Journal of Geodynamics, 43(4-5), 484-503.

Howarth G. H., Sobolev N. V., Pernet-Fisher J. F., Ketcham R. A., Maisano J. A., Pokhilenko L. N., Taylor D. & Taylor L. A. (2015). 3-D X-ray tomography of diamondiferous mantle eclogite xenoliths, Siberia: A review. Journal of Asian Earth Sciences 101, 39–67.

Hughes, H. S., McDonald, I., Faithfull, J. W., Upton, B. G., & Loocke, M. (2016). Cobalt and precious metals in sulfides of peridotite xenoliths and inferences concerning their distribution according to geodynamic environment: a case study from the Scottish lithospheric mantle. Lithos, 240, 202-227.

Hughes, H. S., McDonald, I., Loocke, M., Butler, I. B., Upton, B. G., & Faithfull, J. W. (2017). Paradoxical co-existing base metal sulfides in the mantle: The multi-event record preserved in Loch Roag peridotite xenoliths, North Atlantic Craton. Lithos, 276, 103-121.

Ketcham, R.A., Carlson, W.D. (2001). Acquisition, optimization and interpretation of X-ray computed tomographic imagery: applications to the geosciences. Computers & Geosciences 27, 381-400.

Kiseeva E. S., Kamenetsky V. S., Yaxley G. M., Shee S. R.. (2017). Mantle melting versus mantle metasomatism – “The chicken or the egg” dilemma. Chemical Geology 455, 120-130.

Kohler T.P., Brey G.P. (1990). Calcium exchange between olivine and clinopyroxene calibrated as a geothermobarometer for natural peridotites from 2 to 60 kb with applications. Geochim Cosmochim Acta 54: 2375-2388.

Kyle, J. R., & Ketcham, R. A. (2015). Application of high resolution X-ray computed tomography to mineral deposit origin, evaluation, and processing. Ore Geology Reviews, 65, 821-839.

Lahmer, M. C., Seddiki, A., Zerka, M., Cottin, J. Y., & Tabeliouna, M. (2018). Metasomatism and origin of glass in the lithospheric mantle xenoliths beneath Ain Temouchent area (North-West Algeria). Arabian Journal of Geosciences, 11(12), 1-16.

Lenaz, D., Youbi, N., De Min, A., Boumehdi, M. A., & Ben Abbou, M. (2014). Low intra-crystalline closure temperatures of Cr-bearing spinels from the mantle xenoliths of the Middle Atlas Neogene-Quaternary Volcanic Field (Morocco): Mineralogical evidence of a cooler mantle beneath the West African Craton. American Mineralogist, 99(2-3), 267-275.

Lenaz, D., Musco, M. E., Petrelli, M., Caldeira, R., De Min, A., Marzoli, A., ... & Youbi, N. (2017). Restitic or not? Insights from trace element content and crystal—Structure of spinels in African mantle xenoliths. Lithos, 278, 464-476.

Lenaz, D., Princivalle, F., De Min, A., Petrelli, M., Caldeira, R., Marzoli, A., ... & Said, I. A. A. B. (2019). A comparison between the sub-continental lithospheric mantle of Libya, Morocco and Cameroon: Evidences from structural data and trace element of mantle xenolith Cr-diopsides. Journal of African Earth Sciences, 158, 103521.

Le Roux, V., Bodinier, J. L., Tommasi, A., Alard, O., Dautria, J. M., Vauchez, A., & Riches, A. J. V. (2007). The Lherz spinel lherzolite: refertilized rather than pristine mantle. Earth and Planetary Science Letters, 259(3-4), 599-612.

Logvinova, A.M., Taylor, L.A., Fedorova, E.N., Yelisseyev, A.P., Wirth, R., Howarth, G., Reutsky, V.N., Sobolev, N.V. (2015). A unique diamondiferous peridotite xenolith from the Udachnaya kimberlite pipe, Yakutia: role of subduction in diamond formation. Russian Geology and Geophysics, 56(1-2), 306–320

Lopes, R. P., & Ulbrich, M. N. C. (2015). Geochemistry of the alkaline volcanicsubvolcanic rocks of the Fernando de Noronha Archipelago, southern Atlantic Ocean. Brazilian Journal of Geology, 45(2), 307-333.

Lorand, J. P. (1991). Sulfide petrology and sulphur geochemistry of orogenic lherzolites: a comparative study of the Pyrenean bodies (France) and the Lanzo Massif (Italy). Journal of Petrology, (2), 77-95.

Mancini, L., Dreossi, D., Fava, C., Sodini, N., Tromba, G., Faretto, S., and Montanari, F. (2007). TOMOLAB: The new X-ray microtomography facility @ ELETTRA: Elettra Highlights 2006–2007.

Matsumoto, I., & Arai, S. (2001). Morphological and chemical variations of chromian spinel in dunite-harzburgite complexes from the Sangun zone (SW Japan): implications for mantle/melt reaction and chromitite formation processes. Mineralogy and Petrology, 73(4), 305-323.

Mazzucchelli, M., Rivalenti, G., Brunelli, D., Zanetti, A., & Boari, E. (2009). Formation of highly refractory dunite by focused percolation of pyroxenite-derived melt in the Balmuccia peridotite massif (Italy). Journal of Petrology, 50(7), 1205-1233.

Mercier J.-C.C. & Nicolas A. (1975). Textures and fabrics of upper-mantle peridotites as illustrated by xenoliths from basalts. Journal of Petrology 16, 454-487.

Miller, C. H., Zanetti, A., Thöni, M., Konzett, J., & Klötzli, U. (2012). Mafic and silica-rich glasses in mantle xenoliths from Wau-en-Namus, Libya: Textural and geochemical evidence for peridotite–melt reactions. Lithos, 128, 11-26.

Paganin, D., Mayo, S. C., Gureyev, T. E., Miller, P. R., & Wilkins, S. W. (2002). Simultaneous phase and amplitude extraction from a single defocused image of a homogeneous object. Journal of microscopy, 206(1), 33-40.

Patkó, L., Créon, L., Kovács, Z., Liptai, N., Rosenberg, E., & Szabó, C. (2020). Three-dimensional distribution of glass and vesicles in metasomatized xenoliths: A micro-CT case study from Nógrád–Gömör Volcanic Field (Northern Pannonian Basin). Geologica carpathica, 71(5), 418-423.

Pearson, D.G., Canil, D., & Shirey, S.B. (2003). Mantle samples included in volcanic rocks: xenoliths and diamonds. TrGeo, 2, 568.

Perlingeiro, G., Vasconcelos, P. M., Knesel, K. M., Thiede, D. S., & Cordani, U. G. (2013). 40Ar/39Ar geochronology of the Fernando de Noronha Archipelago and implications for the origin of alkaline volcanism in the NE Brazil. Journal of Volcanology and Geothermal Research, 249, 140-154.

Pike, J. E., & Schwarzman, E. C. (1977). Classification of textures in ultramafic xenoliths. The Journal of Geology, 85(1), 49-61.

Polacci, M., Baker, D. R., Mancini, L., Favretto, S., & Hill, R. J. (2009). Vesiculation in magmas from Stromboli and implications for normal Strombolian activity and paroxysmal explosions in basaltic systems. Journal of Geophysical Research: Solid Earth, 114(B1).

Princivalle F., Salviulo G., Fabro C., Demarchi G. (1994). Inter- and intra-crystalline temperature and pressure estimates on pyrox- enes from NE Brazil mantle xenoliths. Contrib Mineral Petrol 116: 1±6

Pukelsheim, F. (1994). The Three Sigma Rule. The American Statistician, 48(2), 88-91.

Ringwood, A.E. (1991). Phase transformations and their bearing on the constitution and dynamics of the mantle. Geochimica et Cosmochimica Acta, 55(8), 2083-2110.

Rivalenti, G., Mazzucchelli, M., Girardi, V. A., Vannucci, R., Barbieri, M. A., Zanetti, A., & Goldstein, S. L. (2000). Composition and processes of the mantle lithosphere in northeastern Brazil and Fernando de Noronha: evidence from mantle xenoliths. Contributions to Mineralogy and Petrology, 138(4), 308-325.

Sheldrick, T. C., Hahn, G., Ducea, M. N., Stoica, A. M., Constenius, K., & Heizler, M. (2020). Peridotite versus pyroxenite input in Mongolian Mesozoic-Cenozoic lavas, and dykes. Lithos, 376, 105747.

Schneider, C. A., Rasband, W. S., & Eliceiri, K. W. (2012). NIH Image to ImageJ: 25 years of image analysis. Nature methods, 9(7), 671-675.

Swan, A. R., & Sandilands, M. (1995). Introduction to geological data analysis. In International Journal of Rock Mechanics and Mining Sciences and Geomechanics Abstracts (Vol. 8, No. 32, p. 387A).

Szabó, C., & Bodnar, R. J. (1995). Chemistry and origin of mantle sulfides in spinel peridotite xenoliths from alkaline basaltic lavas, Nógraád-Go¨ mo¨ r Volcanic Field, northern Hungary and southern Slovakia. Geochimica et Cosmochimica Acta, 59(19), 3917-3927.

Tabor, B. E., & Downes, H. (2019). Textures of mantle peridotite rocks revisited. Lithos, 348, 105203.

Troll V.R., Klügel A., Longpré M-, Burchardt S., Deegan F.M., Carracedo J.C., Wiesmaier S., Kueppers U., Dahren B., Blythe L.S., Hansteen T.H., Freda C., Budd D.A., Jolis E.M., Jonsson E., Meade F.C., Harris C., Berg S.E., Mancini L., Polacci M., Pedroza K. (2012). Floating stones off El Hierro, Canary Islands: xenoliths of pre-island sedimentary origin in the early products of the October 2011 eruption, Solid Earth, 3, 97-110.

Tromba, G., Longo, R., Abrami, A., Arfell,i F., Astolfo, A., Bregant, P., Brun, F., Casarin, K., Chenda, V., Dreossi, D., Hola, M., Kaiser, J., Mancini, L., Menk, R.H., Quai, E., Quaia, E., Rigon, L., Rokvic, T., Sodini, N., Sanabor, D., Schultke, E., Tonutti, M., Vascotto, A., Zanconati, F., Cova, M., Castelli, E. (2010). The SYRMEP Beamline of Elettra: Clinical Mammography and Bio-medical Applications. AIP Conference Proceedings, 1266, 18-23.

Tuniz, C., Bernardini, F., Cicuttin, A., Crespo, M. L., Dreossi, D., Gianoncelli, A., ... & Zanolli, C. (2013). The ICTP-Elettra X-ray laboratory for cultural heritage and archaeology. Nuclear Instruments and Methods in Physics Research Section A: Accelerators, Spectrometers, Detectors and Associated Equipment, 711, 106-110.

Van Aarle, W., Palenstijn, W.J., De Beenhouwer, J., Altantzis, T., Bals, S., Batenburg, K.J., and Sijbers, J. (2015). The ASTRA Toolbox: A platform for advanced algorithm development in electron tomography. Ultramicroscopy, 157, 35-47.

Wang, Z., Jin, Z., Mungall, J. E., & Xiao, X. (2020). Transport of coexisting Ni-Cu sulfide liquid and silicate melt in partially molten peridotite. Earth and Planetary Science Letters, 536, 116162.

Wells P. (1977). Pyroxene thermometry in simple and complex systems. Contrib Mineral Petrol 42: 109±124.

Wilkins, S.V., Gureyev, T.E., Gao, D., Pogany, A., and Stevenson, A.W. (1996). Phase-contrast imaging using polychromatic hard X-rays. Nature 384, 335–338.

Yao Y., Takazawa E., Chatterjee S., Rihard A., Morlot C., Créon L., Al-Busaidi S., Michinayashi K. & Oman Drilling Project Science Team. (2020). High resolution X–ray computed tomography and scanning electron microscopy studies of multiphase solid inclusions in Oman podiform chromitite: implications for post–entrapment modification. Journal of Mineralogical and Petrological Sciences 191008.

Yarmolyuk, V. V., Kudryashova, E. A., & Kozlovsky, A. M. (2019). Late stages in the evolution of the Late Mesozoic East Mongolian Volcanic areal: rock age and composition. In Doklady Earth Sciences (Vol. 487, No. 1, pp. 773-777). Pleiades Publishing.

Yaxley, G. M., & Kamenetsky, V. (1999). In situ origin for glass in mantle xenoliths from southeastern Australia: insights from trace element compositions of glasses and metasomatic phases. Earth and Planetary Science Letters, 172(1-2), 97-109.

Zandomeneghi, D., Voltolini, M., Mancini, L., Brun, F., Dreossi, D., & Polacci, M. (2010). Quantitative analysis of X-ray microtomography images of geomaterials: Application to volcanic rocks. Geosphere, 6(6), 793-804.

# Figure captions

Figure 1: A) Thin section of mantle xenolith MG10x in plane-polarized light; B) detail of some fluid inclusion trails; C) sulfide crystal included in olivine.

Figure 2: A) 3D reconstruction of sample MG10x obtained at step A (see text and Table 1), 1147x921x1796 voxels. Spinel segmented in orange and sulfides in green; B) 3D reconstruction of a volume of interest in sample MG10x obtained at step B (see text and Table 1), 2004x1536x1240 voxels. Analyses were carried out at TomoLab with a voxel size of 10 micron. Spinel segmented in orange, sulfides in green; C) 3D reconstruction of a volume of interest in sample MG10x obtained at step C (see text and Table 1), 1585x1453x3322 voxels and zooms on some sulfide grains segmented in green.

Figure 3: 3D reconstruction of a volume of interest in sample MG10x obtained at step C (see text and Table 1), 1585x1453x3322 voxels. The red phase is serpentine, which fills fractures and intergranular spaces.

Figure 4: Thin section (A) of sample Bi4 and optical microscope images in plane-polarized light. B) and C): notice the microcrystalline bleb surrounding spinel.

Figure 5: A) 3D reconstruction of mantle xenolith Bi4 obtained at step A (see text and Table 1), 726x660x1969 voxels. Spinel is segmented in orange, voids in blue and high-density phases in green. Insets showing a detail of a spinel cluster and a detail of the high-density phase

alignment at the top of the sample; B) one of the slices composing the 3D model of mantle xenolith Bi4 obtained at step B (see text and Table 1); C) 3D reconstruction of a volume of interest in mantle xenolith Bi4 (step B, see text and Table 1), 1519x1058x1245 voxels. Spinel segmented in orange, voids in blue and high-density phases in green; D) 3D reconstruction of a volume of interest in mantle xenolith Bi4 obtained at step C (see text and Table 1), 1833x1949x1852 voxels. Spinel segmented in orange, voids in blue and high-density phases in green. Insets showing a detail of voids and high-density phases crystallized inside fractures and a detail of the high-density phases at the top of our sample; E) One of the slices composing the 3D model of step C. Arrow indicating a high-density phase crystallized inside a fracture (see Fig.5D). Circle highlighting a microcrystalline bleb surrounding spinel (Sp); F) 3D reconstruction of a volume of interest in mantle xenolith Bi4 obtained at step D (see text and Table 1), 1865x1865x2048 voxels. High-density phases are segmented in green.

Figure 6: Thin section of mantle xenolith FN38 (A) and details of glassy patches with neoblasts crystallized inside (B and C) in plane-polarized light.

Figure 7: A) 3D reconstruction of mantle xenolith FN38 obtained at step A (see text and Table 1), 1121x764x2151 voxels. Spinel segmented in orange, glass in blue; B) 3D reconstruction of a volume of interest in mantle xenolith FN38 obtained at step B (see text and Table 1), 1970x1700x1256 voxels. Spinel segmented in orange, glass in blue. In the upper left corner one of the slices composing the 3D model; notice the absence of spinel (white) inside glassy patches (dark grey); C) 3D reconstruction of a volume of interest in mantle xenolith FN38 obtained at step C (see text and Table 1), 1953x1705x1852 voxels. Spinel segmented in orange. Notice the presence of larger spinel crystals and smaller spinel neoblasts; D) 3D reconstruction of a volume of interest in mantle xenolith FN38 obtained at step D (see text and Table 1), 1825x1833x2048 voxels. Spinel segmented in orange, glass in blue. Arrows pointing at glass filling the intergrain space.

Figure 8: Results of the simulation on 50000 random sections taken in the 3D models of the xenoliths obtained via ICTP data (steps A in Table1), and relative fit.

Supplementary Figure 1: Graph showing Mean intensity vs. Aspect ratio for the high intensity volumes segmented from the three xenoliths. Data obtained through connected components analysis at step A (see Supplementary Table 1).

Supplementary Figure 2: 3D model obtained at step B for mantle xenolith MG10x. Silicates in light grey, spinel in light orange. Skeleton analysis is visible inside spinel, with colour spectrum ranging from blue (lowest connectivity) to red (highest connectivity). The radius of vertices reflects their connectivity and the edge radius reflects the Euclidean length of edges.

Supplementary Figure 3: 3D model obtained at step A for mantle xenolith Bi4. Silicates in light grey. Here is the subdivision of high-intensity ROI into A) low Volume/Surface ratio (in yellow); B) high volume/surface ratio (in black). Notice how yellow highlighted volumes match spinel of Fig.5A.

Supplementary Figure 4: A) 3D model obtained at step A for mantle xenolith FN38. Glass in light blue, silicates in light grey. B) inset showing skeleton analysis inside glasses, with colour spectrum ranging from blue (lowest connectivity) to red (highest connectivity). Radius of vertices reflecting their connectivity and edge radius reflecting Euclidean length of edges.

Fig.1

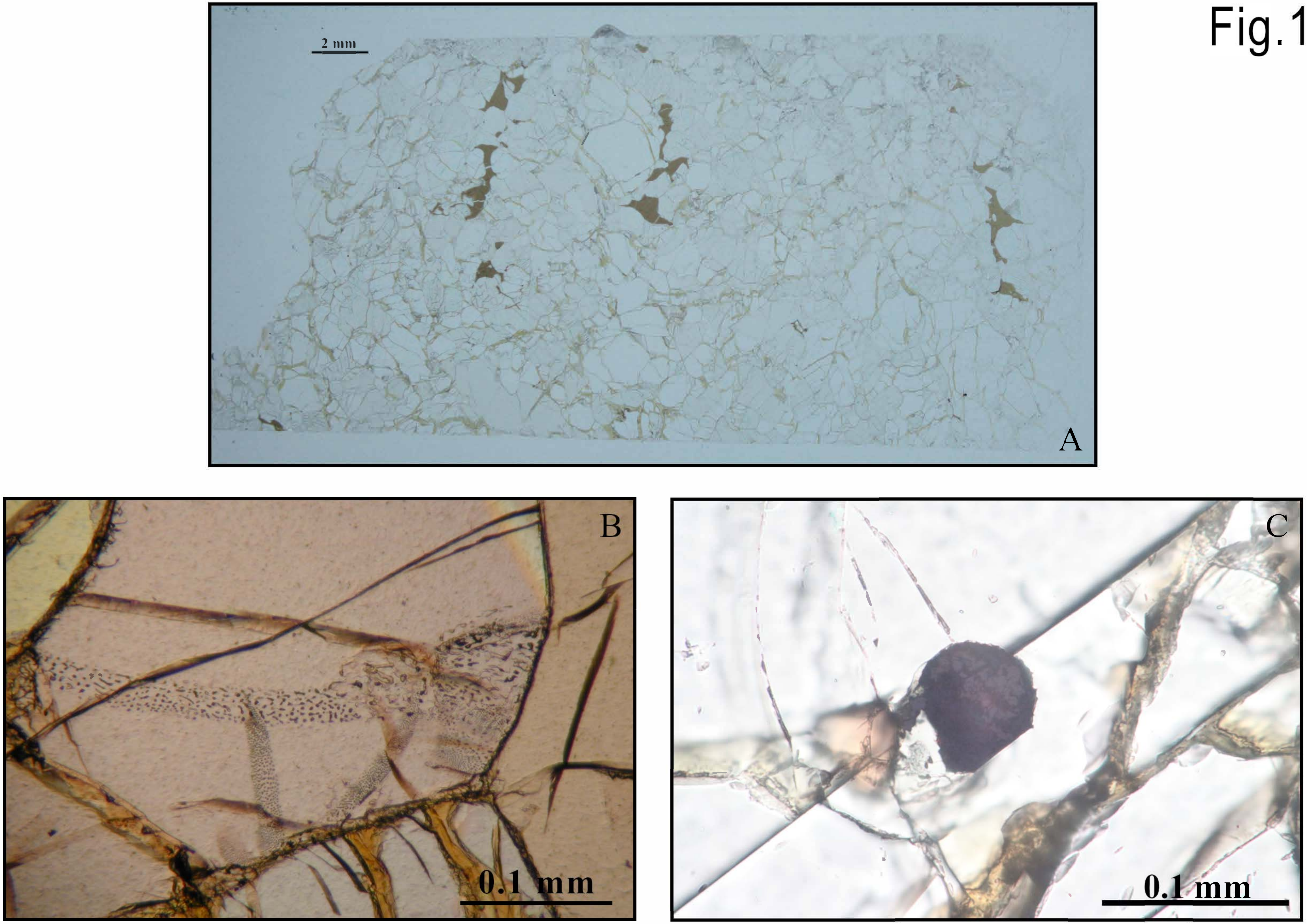

Fig.2

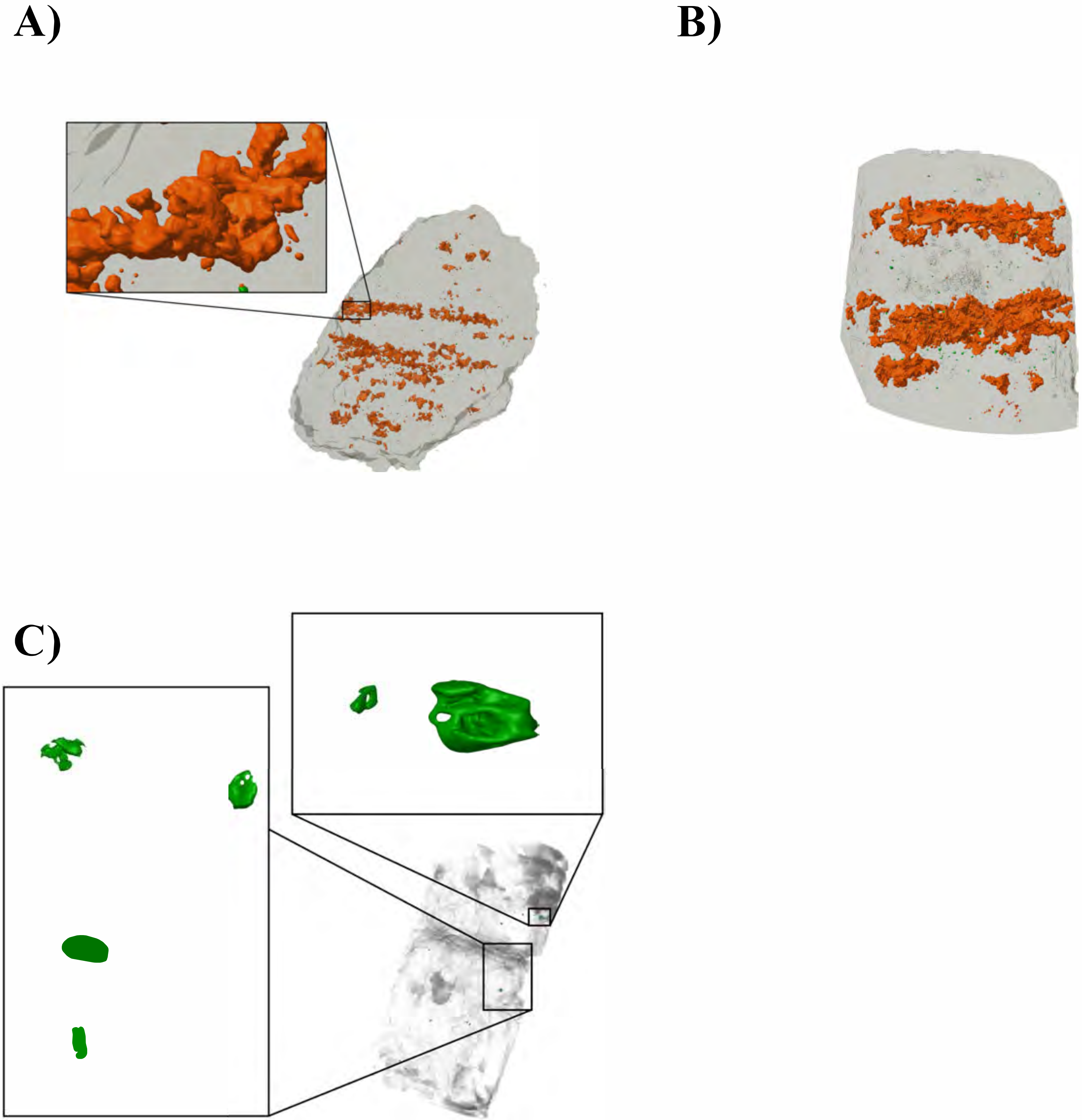

Fig.4

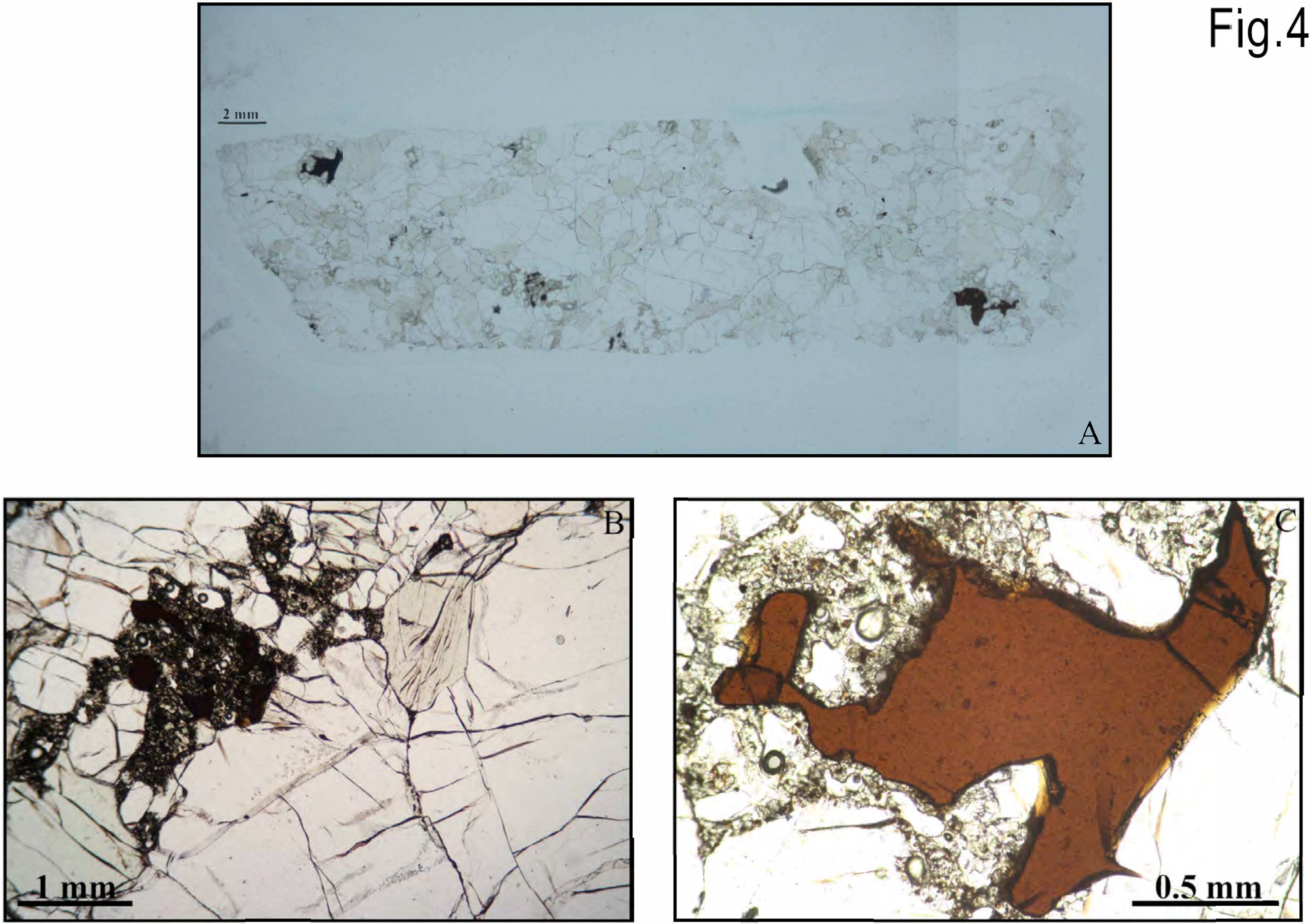

Fig.5

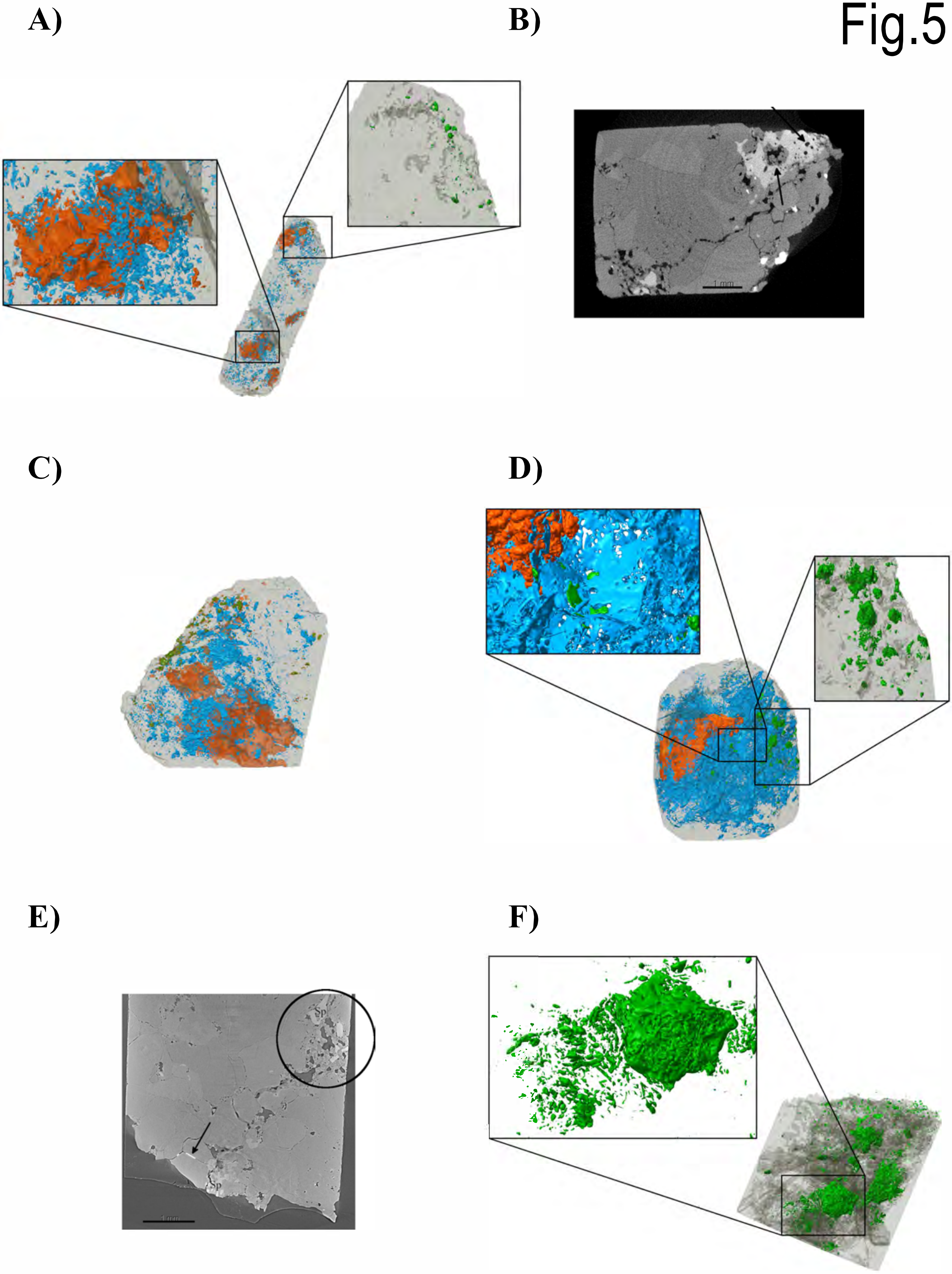

Fig.6

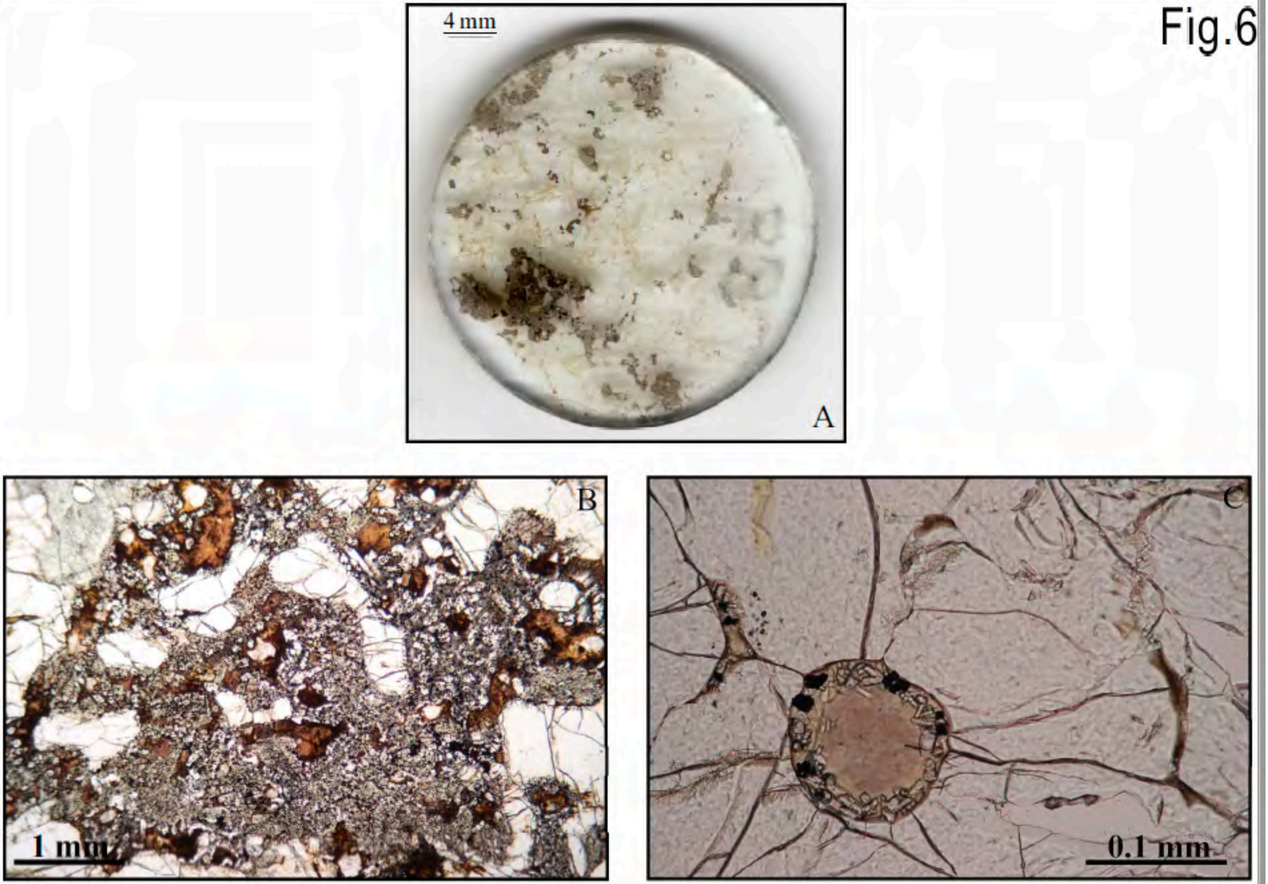

Fig. 7

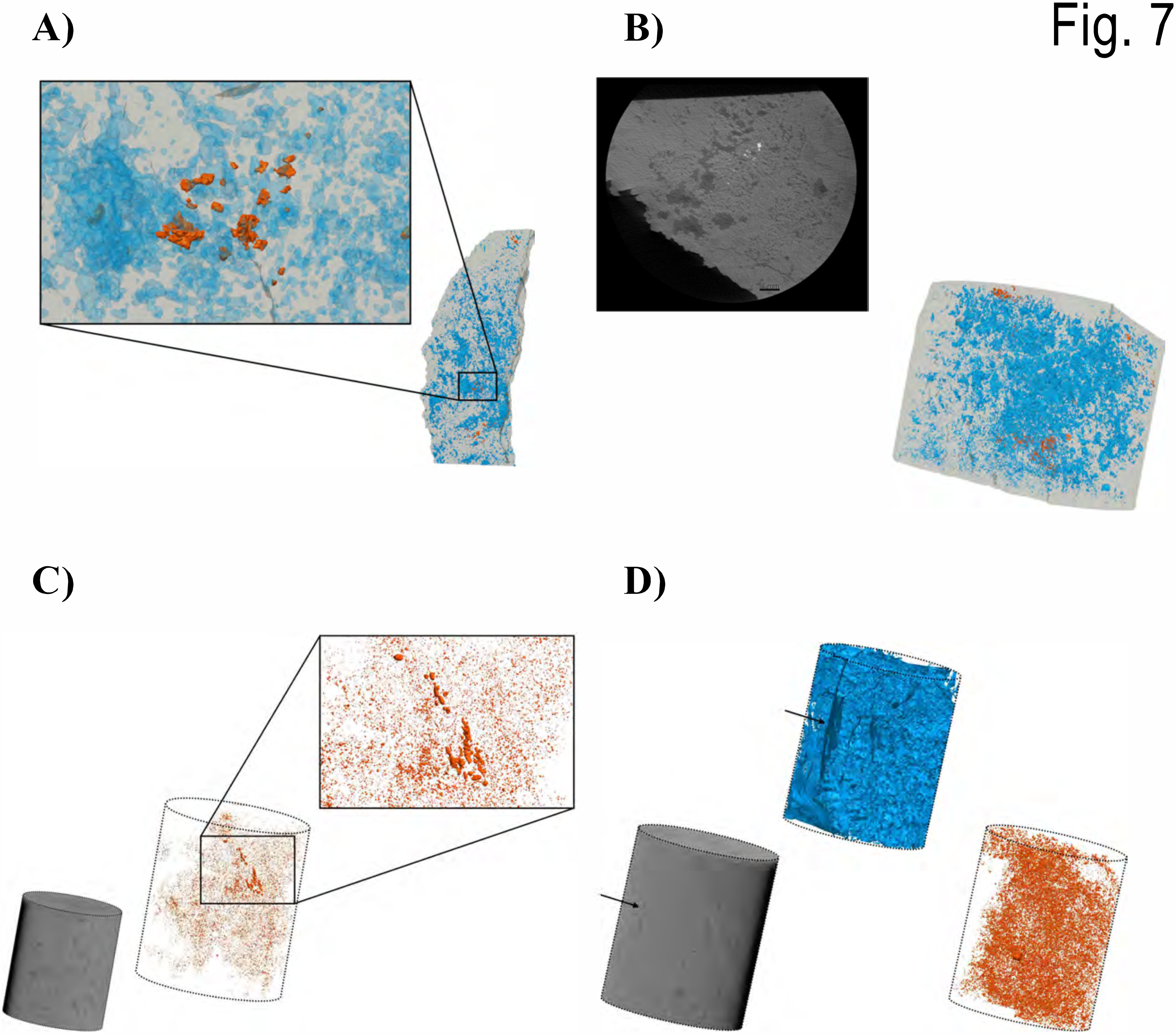

Fig.8

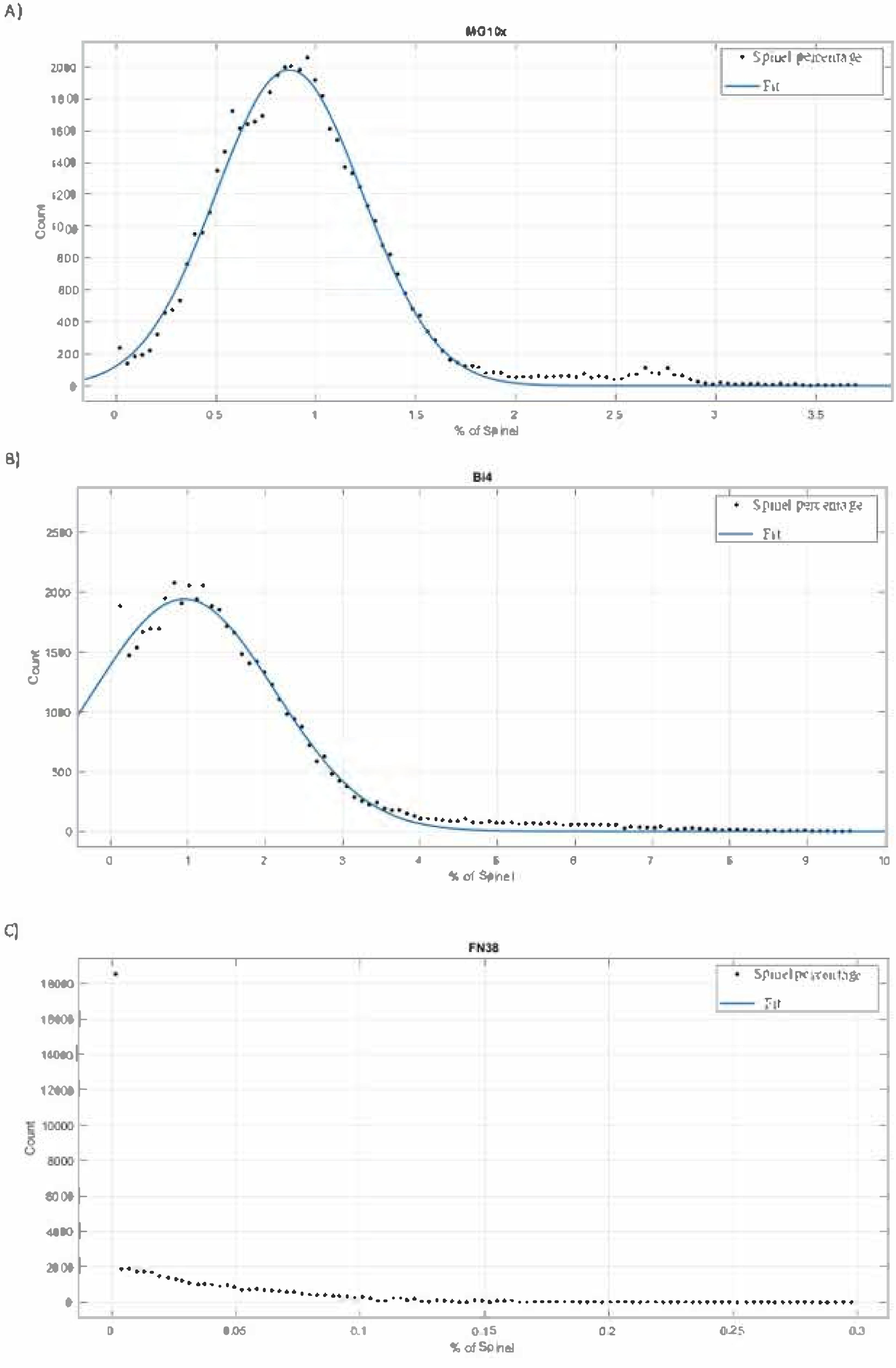
A)
MG10x
Spinel percentage
Fit
Count
0
200
400
600
800
1000
1200
1400
1600
1800
2000
0
0.5
1
1.5
2
2.5
3
3.5
% of Spinel
B)
Bi4
Spinel percentage
Fit
Count
0
500
1000
1500
2000
2500
0
1
2
3
4
5
6
7
8
9
10
% of Spinel
C)
FN38
Spinel percentage
Fit
Count
0
2000
4000
6000
8000
10000
12000
14000
16000
18000
0
0.05
0.1
0.15
0.2
0.25
0.3
% of Spinel